Corrosion effects on the capacity and ductility of concrete half-joint bridges

Original
Corrosion effects on the capacity and ductility of concrete half-joint bridges / Rosso, MARCO MARTINO; Asso, Rebecca; Aloisio, Angelo; DI BENEDETTO, Marilisa; Cucuzza, Raffaele; Greco, Rita. - In: CONSTRUCTION AND BUILDING MATERIALS. - ISSN 0950-0618. - 360:(2022), p. 129555. [10.1016/j.conbuildmat.2022.129555]

Publisher:
Elsevier

Published
DOI:10.1016/j.conbuildmat.2022.129555

Corrosion effects on the capacity and ductility of concrete half-joint bridges

Marco Martino Rosso[a], Rebecca Asso[a], Angelo Aloisio[b], Marilisa Di Benedetto[a], Raffaele Cucuzza[a,*], Rita Greco[c]

[a]Politecnico di Torino, DISEG, Dipartimento di Ingegneria Strutturale, Edile e Geotecnica, Corso Duca Degli Abruzzi, 24, Turin, 10128, Italy
[b]Civil Environmental and Architectural Engineering Department, Università degli Studi dell'Aquila, via Giovanni Gronchi 18, L'Aquila, 67100, Italy
[c]Dipartimento di Ingegneria Civile, Ambientale, del Territorio, Edile e di Chimica, Politecnico di Bari, via Edoardo Orabona, 4, Bari, 70126, Italy

Abstract

Monitoring and evaluating the deterioration of structures is one of the most pressing challenges of the last decades. Bridges and overpasses represent a significant percentage of infrastructures requiring ongoing maintenance and monitoring. In this scenario, a typical static solution used in the last century is the Gerber half-joint, obtained by reducing the cross-section of a beam end, supported by the nib of the adjacent beam or abutment. The particular geometry gives many benefits. However, at the same time, it is the origin of damages and failure due to the difficulty to access for inspections, and the proneness to corrosion phenomena. This study estimates the effect of corrosion on the capacity and ductility of two case studies: a half-joint tested by Desnerk et al. used for model calibration and a real-case half-joint. The

---

[*]Corresponding author.
Email address: `raffaele.cucuzza@polito.it` (Raffaele Cucuzza)

Preprint submitted to Construction and Building Materials *September 30, 2022*

author simulated an increasing level of corrosion in the two case studies by reducing the cross-section of the re-bars and modifying the ductility of steel. The analyses showed different behaviour in the two case studies. While the first exhibited a significant reduction of capacity and ductility, the real-case half joint did not show a manifest capacity reduction, still, accompanied by minor embrittlement of the response.

Keywords: Concrete Bridges, Concrete structures, Half-joint, Corrosion Damage, Numerical Analysis, OpenSees

1. Introduction

Articulated concrete bridges are continuous structures with disconnections in specific span sections to make the system isostatic. The structural scheme of these bridges was named after Heinrich Gottfried Gerber. He designed the Hassfurt Brücke bridge: a three-span bridge with two hinges and disconnections at the span central, supported by the cantilever beams. A beam with half-joints possesses a reduced section at its ends, supported by abutments or adjacent beams. The beam can be either simply-supported beams or resting on two cantilevered supports.

This structural scheme gained wide popularity, especially in Italy, due to its multiple advantages. Specifically, the use of prestressed reinforced concrete allowed it to reach high spans and dimensions comparable to steel beams. In addition, the half-joint owns the benefits of isostatic structures: no internal stresses arise from constraint settlements or thermal variations

[1]. Therefore, using half-joints is relevant when the soil properties might lead to differential settlements. Also, in England, between 1960 and 1970, concrete bridges with half-joints were remarkably successful, used in more than four hundred bridges and viaducts [2]. The Gerber structures allow the rotation of the joints in correspondence to the sections with no bending moment. This fact guarantees the bending moment distribution typical of continuous beams. In addition, the joint, behaving like a hinge, allows the transfer of shear and normal stresses between adjacent beams.

Nonetheless, this structural typology has several drawbacks: For example, a single joint's collapse might induce the entire structure's failure as an isostatic structure. Conversely, continuous beams have plastic resources typical of hyperstatic systems. Non secondarily, the joints are not accessible for inspections or interventions. In addition, the reinforcement bars in the joint suffer from corrosion phenomena due to water infiltration [3]. However, although these structures are prone to corrosion phenomena, it is not effortless to retrofit and observe the progress of degradation.

Unfavourable conditions for the preservation of the joints originate from the lack of adequate drainage or waterproofing systems. The infiltration of water and de-icing salts cause the initialisation of the corrosive process of the rebars, leading to a capacity reduction of the entire system [4, 5, 6, 7]. If this effect adds to the difficulty of an efficient maintenance plan, the risk of collapse boosts. Desnerck et al. indicated that in England, 38% of the bridges of this structural type deteriorated due to corrosion [8]. Numerous inspections carried out on these bridges highlighted the half-joint deterioration. For example, in a study by Nicholson T., the examinations conducted in Australia on two bridges proved the relation between water infiltrations and corrosion of the reinforcement bars and concrete deterioration [9, 10, 11]. Other inspections executed in the Medway bridge in England revealed a 50% reduction of the rebar cross-sections [12]. Another remarkable example of half-joint deterioration is the bridge over the Basento River (Italy), designed by Musmeci and built between 1971 and 1976, see Fig.1(a). The half-joints are reinforced with diagonal and horizontal bars, with 30mm diameter, and vertical ones equally spaced with 10mm diameter. The current state of the bridge exhibits evident signs of deterioration, especially in the half-joints, see Fig.1(a). Damage to the bridge is related to inadequate maintenance and repair of drainage systems. This fact led to corrosion of the reinforcement bars with consequent concrete cracking and spalling of the concrete cover [13].

(a) (b)

Figure 1: (a) Detail of the deterioration of the half-joint in the Musmeci bridge [13]. (b) Deterioration of the half-joint due to corrosion before collapse, [14].

The joint geometry affects its degradation: the water stagnates at the connection level, increasing the possibility of bar corrosion. In addition, this system possesses the inherent disadvantage of isostatic systems related to potential catastrophic collapse. A remarkable example of the vulnerability of this structural typology is the collapse of the La Concorde bridge in Quebec (Canada, 2006), built in 1968 and characterized by a central span supported by cantilevered beams with half-joints, see Fig.1(b). The collapse of the viaduct depended on several factors: the bars' misalignment, unsuitable repairs and cracking of the concrete due to corrosion of the reinforcement bars [15, 2]. The above considerations confirm that the absence of adequate monitoring of degradation phenomena can significantly affect the capacity of half-joints. Half-joints possess pros and cons. Therefore, the sensitivity of these structures to corrosion phenomena is crucial, especially given that most of these existing structures have reached their nominal lifetime.

This study estimates the sensitivity of half-joint capacity and ductility to corrosion phenomena from numerical modelling calibrated on experimental tests. The analyses correlate the intensity of corrosion with ductility and capacity losses. A recent related study has been conducted in [16], evidencing how this research topic is still an active field, especially because of many Gerber infrastructures existing heritage which is nowadays approaching to the end of the nominal life. In the current work, the authors focus on two case studies: a half-joint made in a laboratory by Desnerck, Lees and Morley [17] and a half-joint corresponding to an existing viaduct. The two joints were modelled in OpenSees using the scientific toolkit for OpenSees (STKO) software [18]. The first model is also used for calibration using the experimental data by Desnerck et al. A significant aspect of this research's originality is comparing the effect of corrosion in two case studies to highlight the impact of scaling and prestressing on capacity and ductility reduction due to corrosion. The paper has the following organization. After the case studies presentation and brief literature background, the paper presents the results of numerical simulations for increasing levels of corrosion.

2. Problem formulation and literature background

The geometry of half-joints demands the beam partition into two regions, defined as B and D respectively [19], as shown in Fig.2. The B-region (from Bernoulli) comprises the cross-sections where the Bernoulli-Navier hypothesis can be considered valid. On the other hand, in the D-regions, the Euler-Bernoulli beam model cannot be applied. The geometric discontinuity leads to a two or three-dimensional stress state, which deserves a specific formulation.

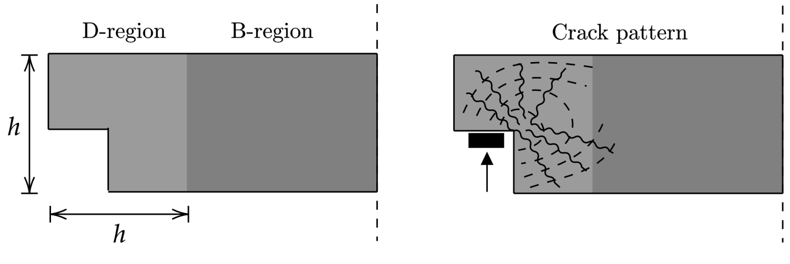

Figure 2: Detection of D-region and B-region in a half-joint.

Several authors studied the half-joint, looking for a reliable and effective design system [20]. Numerous codes allow the design of this joint. See the PCI, ACI, and British Standard [21, 22]. However, no research investigated the different levels of accuracy of each approach. A widely used design method is the Strut & Tie (S&T) method, which allows the design of discontinuity zones or D-regions based on the equivalent truss concept [23, 24]. The equivalent truss model is generally applied to the B-regions. Currently, the model has also been extended to the calculation and design of the D-regions.

Many researchers devised different reticular models to determine the optimum reinforcement layout and the parameters affecting the half-joint behaviour. In 1979 Mattock and Chan [25] were among the first to study the half-joints, proposing an alternative design strategy. A later model, developed by Liem in 1983 [26], introduced a diagonal bar in the rebound zone. The study showed that a half-joint with bars inclined at 45° presented a resistance two times higher than one with horizontal or vertical bars [26]. In 2003 Lu et al. [27] piloted further studies on half-joints, analyzing the parameters that most influence their behaviour, including the strength of concrete and the configuration of the re-bars. The results of the tests showed that by increasing the characteristic strength of the concrete and the quantity of horizontal reinforcing bars, the capacity increased [27]. Another study by Desnerck et al. in 2016 assessed the sensitivity of the half-joints capacity to the re-bar configuration. They highlighted that the absence of U-bars led to a minor reduction of the bearing capacity and a brittle failure. Conversely, the lack of diagonal bars resulted in a substantial decrease in the overall strength (about 39%) [28].

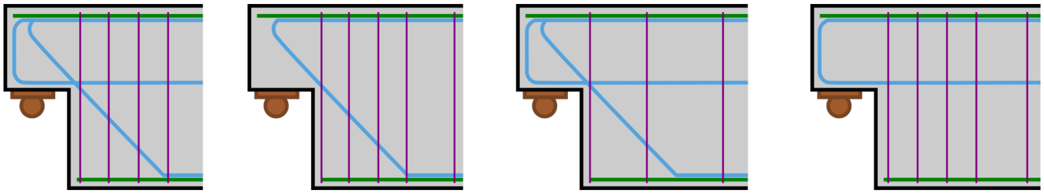

Figure 3: Reinforcement configurations of the different specimens studied by Desnerck et al., [28].

Desnerck [2] performed laboratory analyses on half-joints, evaluating the deterioration state and the response variation due to different levels of corrosion. He found that a 40% reduction of the re-bars cross-sections led to a 20% decrease in the half-joint capacity [2, 28]. In 2021, Santarsiero et al. [13] carried out a mechanical-chemical analysis on the effect of chloride attack corrosion on a half-joint of an existing viaduct. They measured the concentration of chlorides at different depths. They found that 45 years after construction, there is a 6% loss of strength, while an 18% reduction in the peak strength can be observed after 95 years [13].

2.1. Description of the case studies

The first half-joint model developed in this paper is based on the configurations tested by Desnderck [2]. The experimental data allowed the calibration of the FE model. The joint is reinforced with ordinary reinforcement bars and does not possess prestressing cables, see Fig.4. The reinforcement includes five upper and lowers longitudinal bars to ensure flexural strength.

U-bars and diagonal bars have also been used to comply with the classic Strut and Tie models. In addition, there are stirrups for absorbing shear stresses [29]. Fig.4 shows the geometry of the joint [28].

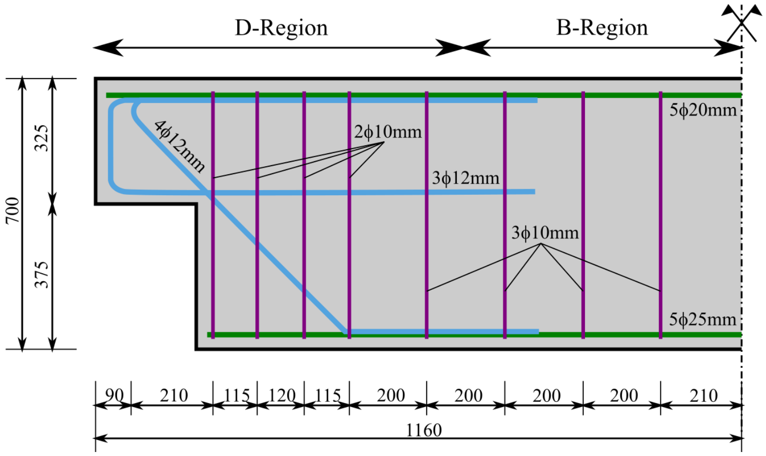

Figure 4: Geometry of the Gerber joint, NS_REF specimen [28].

The experimental beam was tested with a three-point bending test. The experiment is based on two consecutive phases: the force gradually increased until the first half-joint reached failure. Then, after unloading, the load is increased again until the second half-joint fails [28]. In Desnerck et al. [28], it was mentioned that the 10 mm or 12 mm diameter reinforcements cold deformed to match the required design steel arrangement of the experimental testing, while the larger diameter bars were hot rolled. However, since the hardening is probably concentrated in the bent area for diagonal bars and stirrups, the authors adopted an elastic-hardening stress-strain law for all the uncorroded rebars. For the corroded ones, according to [30], the authors adopted an idealized three-linear law as elastic-hardening and a post-peak

Table 1: Material properties.

Concrete

Description	Label	Value	Unit
Cubic compressive strength	$f_{c,cub}$	47.6	MPa
Cylidric compressive strength	$f_{c,cyl}$	33.8	MPa
Flexural compressive strength	$f_{c,fl}$	3.71	MPa
Young's modulus	E_c	33000	MPa
Steel			
Yielding strength for phi10	f_y	539	MPa
Yielding strength for phi12	f_y	529	MPa
Yielding strength for phi20-25	f_y	578	MPa
Young's modulus	E_s	210000	MPa
Supports			
Young's modulus	E_s	210000	MPa
Poisson ratio	ν	0.3	

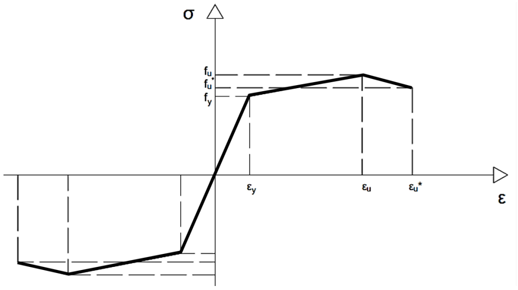

Figure 5: Idealized stress strain law for corroded rebars.

linear decreasing law until reaching the ultimate deformation, as illustrated in Fig. 5. This law was adopted in order to catch also the ductility reduction of the corroded rebars, as explained in section 2.3 of the present document. Tab.1 summarizes the characteristics of the materials used for the FE model [28].

The second case study refers to an existing viaduct built in 1990, composed of a prestressed solid slab deck with post-tensioned cables. The structure has a 35 m span with two longitudinal overhangs, see Fig.6. The deck has a constant cross-section and was made from on-site cast concrete. Fig.6 shows the geomteric details of the second case study.

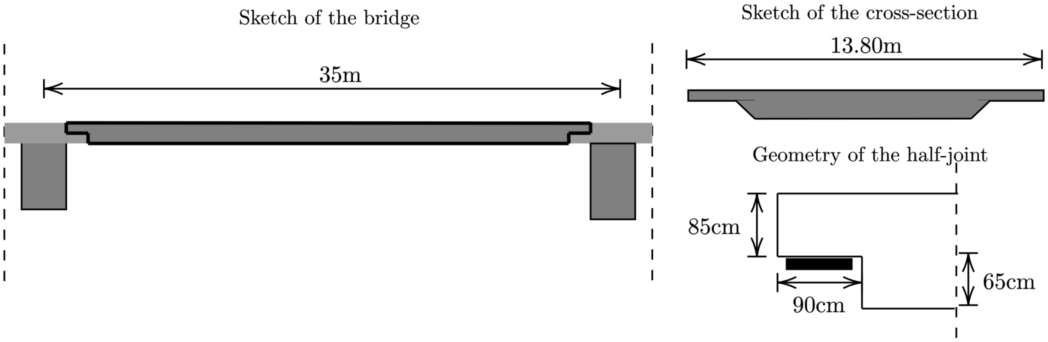

Figure 6: Sketch of the existing bridge.

Table 2: Properties of the materials.

Concrete

Description	Label	Value	Unit
Cubic compressive strength	R_{ck}	45	MPa
Cylindric compressive strength	f_{ck}	35	MPa
Tensile strength	f_{ctm}	3.21	MPa
Young's modulus	E_{cm}	34077	MPa
FeB44k Steel			
Yielding strength	f_{yk}	430	MPa
Ultimate strength	f_{tk}	540	MPa
Young's modulus	E_s	210000	MPa
Harmonic steel			
Yielding strength	f_{tpk}	1800	MPa
Strength at 0.1% deformation	f_{tyk}	1620	Mpa
Young's modulus	E_s	195000	MPa

Tab.2 summarizes the characteristics of the materials used for the FE model [28].

2.2. FE modeling of the half-joints

The STKO toolkit is an advanced graphic user interface (GUI) for OpenSees [18], used to analyze different types of structures. The adoption of STKO software within the current research was firstly motivated by the advantage that this software overcame the limitations of working without a GUI in the traditional OpenSees pipeline, while still providing all the powerful and extensive tools for nonlinear structural analysis implemented in the OpenSees open source framework. The software is interoperable, permitting the exportation of the compiled database of the FE model (materials, geometry, constraints, etc.) in the tool command language (TCL), which could be also executed in the traditional OpenSees way [18]. Moreover, in the current study, the STKO software permitted a simpler managing of non-linear analysis of complex models with an automatic multi-processor execution, exploiting the computational capabilities of the adopted computer architecture, thus considerably reducing the computational time and effort. It is worth recalling that, in OpenSees, the FE model is an aggregation of components (objects in computer science terminology) defining the geometry, the analysis, the load patterns, etc [31]. Therefore, since STKO followed the same logic as OpenSees, the main limitation of the software is represented by an initial unhandy usage of the software by OpenSees non-expert users, thus requiring a substantial starting learning phase to understand how to effectively govern the OpenSees working pipeline. STKO is divided into two sections, pre-processing and post-processing, allowing the user to control all process phases. The interface with the Python writing language allows the user to customize and program pre and post-processing operations according to personal needs [18]. In the pre-processing phase, the following input parameters are defined:

- The geometric model of the structure;
- The reinforcement bars, using wire elements;
- The materials, through the physical properties module. The constitutive law of materials is non-linear and is based on the mechanics of fracture and shown in the following paragraphs;
- The constraint conditions, through the Interaction and Condition modules;
- The load conditions, through the Condition module which allows applying concentrated, distributed, volume loads or displacements and deformations;
- The mesh, by assigning the number of divisions or the characteristic size.
- The steps of the analysis through the Analysis module.

In the post-processing phase it is possible to observe all the results of the analysis and extrapolate the information produced: tensions, deformations, stresses, damage, etc.

Reinforced concrete structures have a highly heterogeneous nature. The behaviour of concrete depends on its constituents' physical and chemical properties. Additionally, concrete is also subject to micro-cracks and areas of discontinuity [32]. Therefore it is necessary to adopt constitutive models able to grasp the non-linearity of the problem, providing simplified representations of the tensile and compressive behaviour of the materials [33]. The constitutive model for the concrete is a damage model with two parameters d^+/d^-, following [34]:

$$\sigma = (1 - d^+)\bar{\sigma}^+ + (1 - d^-)\bar{\sigma}^- \tag{1}$$

where $\bar{\sigma}^+$ and $\bar{\sigma}^-$ are the positive and negative stress tensors. d^+ and d^- indicate the damage indices of concrete in tension and compression, respectively [34, 35, 36]. They influence the calculation of the positive and negative components of the stress tensor. They are scalars in the range 0-1, indicating the deterioration status of the concrete: if the parameter is 0, the material is intact, while if one, the material is wholly damaged [34]. The damage indices $\bar{\sigma}^+$ and $\bar{\sigma}^-$ are obtained from the concrete behaviour in tension and compression, which can be evaluated through the stress-strain curves of the material. The tensile behaviour of the concrete is characterized by a linear elastic phase up to the tensile strength. After the attainment of the tensile strength, the material shows a softening-like trend, i.e. a decrease in resistance as the deformation of the material increases up to complete failure.

The full details of the model are provided by [34].

The model by [34] requires the definition of the fracture energy. Fracture energy is the energy needed to propagate a crack by a unitary quantity [32]. Its value depends on the type of concrete and is necessary to understand the tensile behaviour of concrete. The fracture energy is a critical parameter of concrete, depending on the size and geometry of the specimens. The fracture energy, also known as specific fracture energy, and the tensile strength are intrinsic properties of the materials and can be obtained experimentally through the ASTM and RILEM standards. In the absence of experimental data, the fracture energy G_f can be calculated by referring to the formulations provided by the Model Code 1990 or by the Model Code 2010 [37]:

$$\text{Model code 1990} \rightarrow G_f = G_{f0}\left(\frac{f_{cm}}{f_{cm0}}\right)^{0.7} \tag{2}$$

where $f_{cm0} = 10\text{MPa}$ and G_{f0} is the base value of the fracture energy dependent on the maximum size of the aggregate (d_{max}): 0.025, 0.030 and 0.058 for d_{max} equal to 8, 16 and 32mm, respectively.

$$\text{Model code 2010} \rightarrow G_f = 73 \cdot f_{cm}^{0.18} \tag{3}$$

To provide a better matching with the Desnerck et al. experimental curve, the 1990 formulation is used which leads to lower fracture energy values, assuming a d_{max}=16mm. The calculation of the compression fracture energy is carried out following the "Guidelines for Nonlinear Finite Element Analysis of concrete structures” [38], as follows:

$$G_c = 250 \cdot G_f \tag{4}$$

where G_c is the compression fracture energy. The estimated tensile and compressive fracture energy values are used as input parameters for the constitutive model of the concrete. It is worth recalling that fracture energy depends on many factors, such as concrete physical properties, hydration, and drying processes, and it is also affected by the size and geometry of the specimen. However, in absence of specific experimental testing controlling the hydration and drying processes, it was reasonable for the authors to assume the Model Code formulations for fracture energy. Furthermore, the dependence on the size and geometry of the specimen could also be regarded as a dependence on the discretization level of the model. Thus, considering the following relationship

$$g_f l_{dis} = G_f, \tag{5}$$

G_f represents the fracture energy, g_f is the specific fracture energy per unit of volume, and l_{dis} is the length of the damaged zone, which may be considered equivalent to the characteristic length of each finite element (l_{ch}) i.e. $l_{dis} = l_{ch}$. Therefore, when dealing with discretized problems, it is common to adopt regularized values for fracture energy in tension and consequently even for fracture energy in compression. The adopted software STKO provided to the authors an auto-regularization of the fracture energy from the starting values from Model Code relationships which automatically accounts the implemented geometry of the discretization of the FE model.

Steel has similar behaviour in tension and compression. Therefore the authors adopted a bilinear elastic law: the first phase up to the yield stress (f_y) followed by a hardening phase till the peak tension (f_u). Ultimately, a softening section is adopted, simulating the loss of strength up to the limit strain deformation of steel.

The problem is non-linear type due to the areas of discontinuity and non-linearity of the material. In the FE problem, the solution is obtained by searching an equilibrium configuration at each loading step [39, 40]:

$$R(t) - F^{in}(t) = 0 \tag{6}$$

where $R(t)$ is the vector of the external nodal forces and $F^{in}(t)$ the vector of the internal nodal forces. The approximate equilibrium solution is found using the Newton-Raphson method.

2.3. Corrosion modelling

Corrosion yields numerous effects, including the loss of rebar sections, the variation of the mechanical properties and ductility of the steel, the failure of the steel-concrete bond and the formation of discontinuities and cracks on the concrete surfaces [41, 42, 43, 44]. Furthermore, several authors analysed the corrosion of reinforcement bars issue of concrete bridges, e.g. developing a new Markov chain-based model (see e.g. Dizaj et al. [45] and Lethanh et al. [46]), or incorporating temporal and spatial variations of probabilistic corrosion rate sensor data (Zhao, J. and Niu, D.T. [47], Marsh, P.S. and Frangopol D.M. [48], Yu, B. et al. [49] and Xu, F. et al. [50]). Some other scholars developed both numerical and analytical models aiming to investigate the effect of local corrosion on steel reinforcement bars (e.g. Chen, X. et al. [51]) and non-uniform (Zhu, W. et al. [52]) or to consider collateral corrosion-induced effects, e.g. the enhancement of concrete carbonation issues (Sun, B. et al. [53]) or the cracking of concrete cover (Zhang, K. et al. [54]).

Analyzing all these effects is challenging, also given the difficulty in creating a model including all corrosion phenomena [55, 56, 57, 58, 59]. Therefore, this study takes into account the two main effects of corrosion i.e. the loss of cross-section and the loss of ductility of the rebars [60, 61, 62, 63]. Future developments may also consider more complex simulation, accounting e.g. the changes in the adhesion properties due to corrosion formations.

- **Cross-section reduction**: The authors assume that the effect of corrosion is homogeneously distributed on a specific group of rebars, more prone to corrosion. Therefore, deterministic levels of corrosion are considered from 5% to 50% with a 5% step increment, expressing the average percentage loss of cross-section.

- **Ductility and strength decay**: The ductility loss of the rebars is obtained by modifying the constitutive behaviour of steel. As a result, the resistance and deformation vary with the corrosion percentage, expressed as the average percentage of section reduction, following the relationships by Cairns et al. [64], shown below:

$$f'_y = (1 - \alpha_y Q_{corr}) f_y \tag{7}$$

$$f'_u = (1 - \alpha_u Q_{corr}) f_u \tag{8}$$

$$\epsilon'_u = (1 - \alpha_1 Q_{corr}) \epsilon_u \tag{9}$$

where f'_y, f'_u and ϵ'_u are the yielding strength, ultimate strength and ultimate deformation of steel after corrosion, while f_y, f_u and ϵ_u are the yielding strength, ultimate strength and ultimate deformation of steel before corrosion. Q_{corr} is the average percentage of section reduction, while α_y, α_u and α_1 are empirical coefficients. The empirical coefficients α_y, α_u and α_1 generally derive from literature data, based on the researches by Cairns et al. [64]. The assumed values for α_y, α_u and α_1 are 0.015, 0.013 and 0.017 respectively, after Andrade et al. [65]. Focusing on the stress-strain law for corroded rebars depicted in Fig.5, the values of deformation at the peak strength and the ultimate point at failure have been calibrated based on [30] for each considered corrosion level and each diameter size.

3. 1st case study: half-joint tested by Desnerck et al.

The model calibration in STKO is based on the experimental tests by Desnerck et al. [28]. The authors followed a 3D modelling approach.

3.1. Input parameters

The half-joint is modelled in STKO using solids FE for the concrete beam and load plates, while wire elements for the reinforcement bars. Fig.7 shows some captures of the geometric model in STKO.

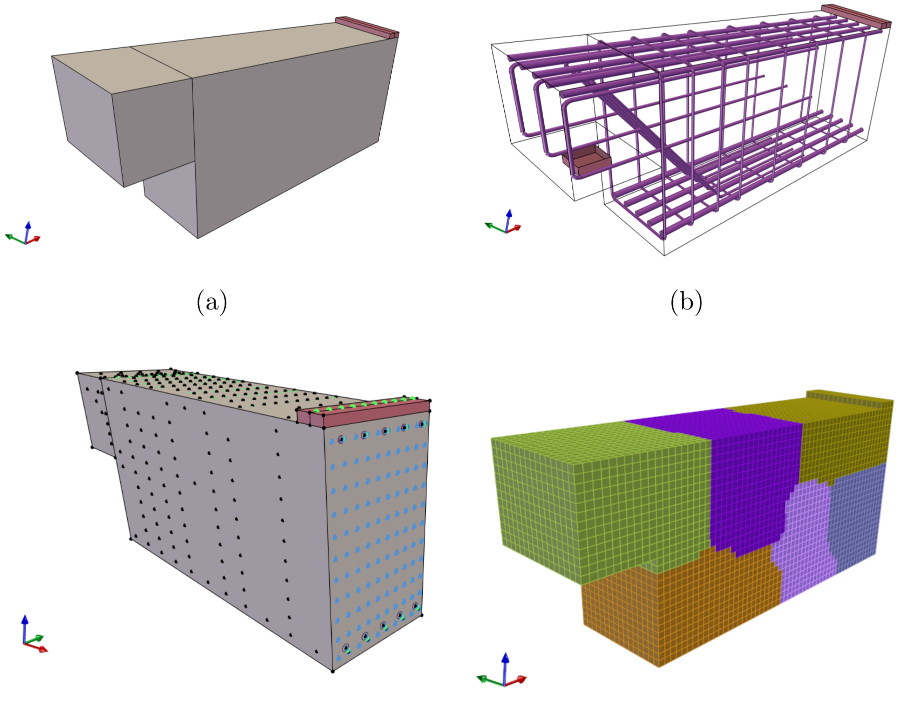
(a) (b)

(c) (d)

Figure 7: (a) 3-d model of the half joint and (b) view of the rebars arrangement; (c) details of the constraint; (d) mesh partition.

For concrete, a *DamageTC3D* type nD material is used, which allows grasping the brittle behaviour of the concrete, as well as its tensile and compressive response by using the values of the tensile and compressive fracture energy calculated following the Model Code 1990 [37]. The compression and tensile fracture energies are equal to 20.56 and 0.082 N/mm respectively.

The fracture energy depends on the structural dimensions and material characteristics, as reported in the Model Code 1990. An initial analysis was carried out with the fracture energy obtained from the MC1990. However, to further reach a better matching with the experimental curve provided in Desnerck et al. 2016 [28], the authors tuned a further 12.5% reduction factor of the initially assumed value. This reduction of the fracture energy in the FE model led to a further reduction of the tensile resistance, estimated as 1.8MPa from the Eurocode 2 relationships between fracture energy and tensile strength.

For steel, a *Hysteretic* material is used. This material is characterized by a uniaxial bilinear hysteretic behavior with pinching of force and deformation, able to model damage both due to ductility and energy, with a possible degraded unloading stiffness based on ductility [31]. The *bbarBrick* element type is adopted to model the entire solid half-joint geometry, the steel plates employed both to apply the load and as well for the supports. A bbarBrick element is referred to as an eight-node mixed solid brick element object which adopts a trilinear iso-parametric formulation [31]. Within the distributed plasticity methods, it is worth recalling that the *fiber section* mechanical modeling technique adopts sections composed of fibers, and every single fiber has a certain cross-section and a certain uniaxial material stress-strain law. Therefore, in the present study, the reinforcing bars are modeled as mono-dimensional *ForceBeamColumn* elements for iterative force-based formulation analysis with assigned a fiber section mechanical model, where to each fiber the previously mentioned stress-strain laws for the various considered diameters for uncorroded or corroded conditions have been assigned [31]. The *node-to-element* link [18], also denoted as *BeamContact3D* [31], is used between the reinforcement bars and the concrete half-joint, reproducing the perfect bonding of the rebars with the surrounding concrete elements, and a penalty is assigned to the constraint equal to the elastic modulus of the concrete.

The constraint conditions are assigned through the condition module: an external support in correspondence with the reduced section prevents the vertical translation. Albeit in the Desnerck et al. 2016 [28] study, two conditions were experimentally tested, one symmetric and one asymmetric due to a different location of the external supports, in the present study the authors only referred to the symmetric case. Thus, similarly to other recent studies, e.g. [66], the authors modelled half of the dapped-end beam leveraging the symmetric condition.The authors modelled half of the dapped-end beam. Therefore, a double pendulum constraint at mid-span prevents the horizontal translation along the x axis and rotation around the y axis [28].

Fig.7 (c) also reveals the load condition. In order to numerically simulate the experimental test conducted by [28], the authors leveraged the symmetry of the three-points bending test by modeling half of Desnerck's beam. A steel plate has been modeled in correspondence with the symmetry section to apply the step-wise vertical load, whereas another steel plate was modeled in correspondence with the nib to represent the external support. The laboratory tests [28] showed that the ultimate displacement, before reaching failure, is 12 mm and that the maximum load reached is 402 kN. Therefore, a distributed stress of 10 MPa is applied by the steel load plate, assigning an ultimate displacement equal to 12mm. Linear and Hexaedric mesh is adopted to discretize the model. A convergence analysis proved that a mesh size equal to 2.5 cm represents a good trade-off between accuracy and computational effort.

3.2. Results in case of no corrosion

This paragraph presents the results of the analysis in case of no corrosion: tensile damage (localization of cracks), deformation of the concrete, and stresses in the reinforcement bars. Fig.8 compares the experimental and numerical estimates for the force-displacement curve by varying the mesh size and discretization step. The agreement with the experimental data is very satisfactory with minor relative error of the peak force and tangent stiffness. The results are shown from the initialization of the cracking process to the damage progress and failure, see Fig.9:

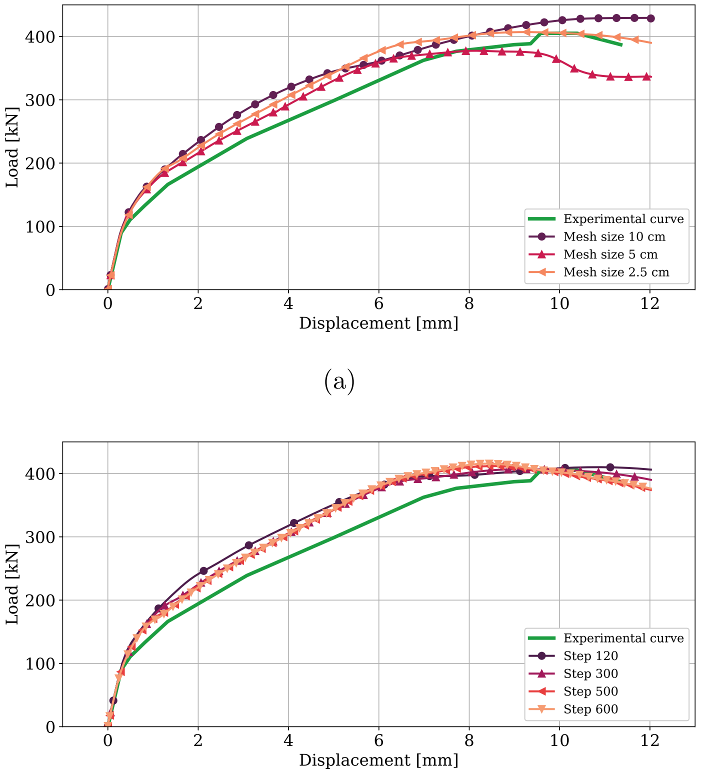

(a)

(b)

Figure 8: Comparison between experimental and numerical prediction of the force displacement curve by considering different mesh sizes (a) and different discretizations for the load steps (b).

- **Tensile damage**: the cracks start to propagate from the inside edge and extend over the entire cross-section. The most critical cracks, however, are those present in the recessed area, which go towards the upper edge of the beam.

- **Minimum deformation of the concrete**: it should be verified that it does not exceed the critical value of 0.35%, below which failure would occur due to the crushing of the concrete, causing a brittle collapse of the joint. The analysis shows that the critical value is never reached at any point. Therefore the failure can be considered ductile.

- **Tension in the reinforcement bars**: the collapse occurs due to the achievement of the yield stress in the diagonal bars and the first two stirrups (see Fig. 10), leading to a ductile failure.

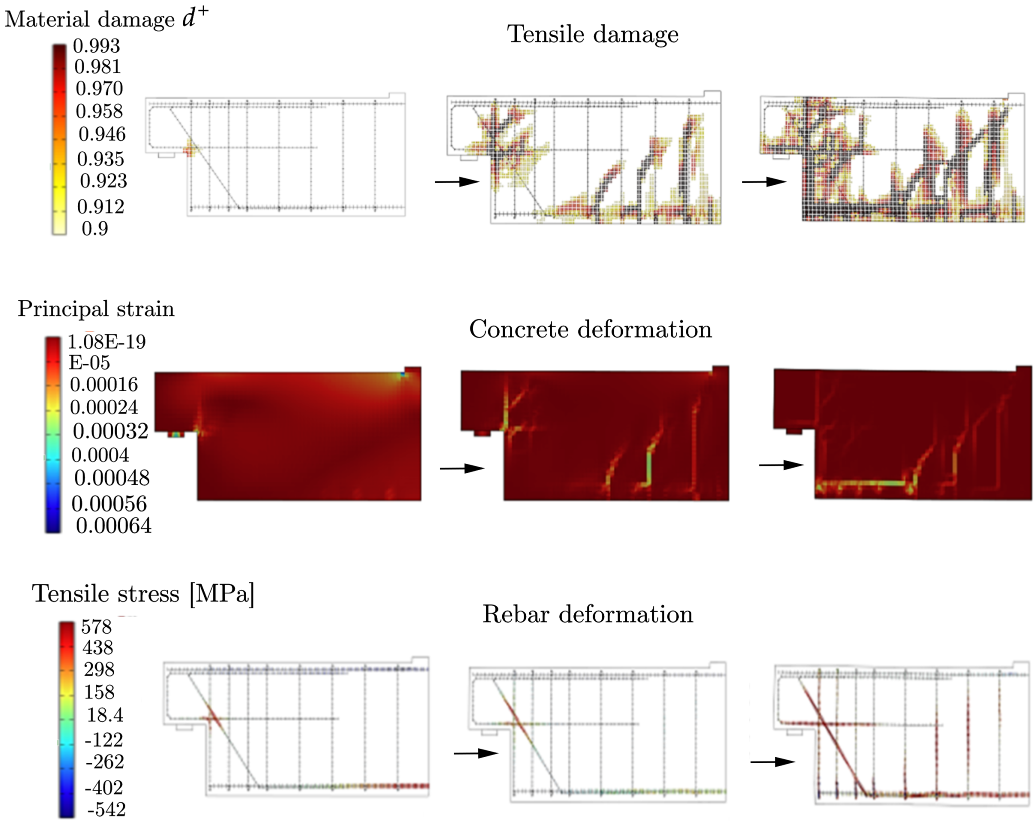

Figure 9: Progress of damage in terms of tensile damage indiex, concrete deformation and stress in the rebars.

3.3. Results in case of corrosion

The half-joint degradation is estimated by localizing the corrosion to the rebars more exposed to it, as shown in Fig.10. These are the rebars more exposed to aggressive agents since the first cracks are located by the cross-section reduction, as highlighted in the previous paragraphs. The effects of corrosion are applied equally to all the considered bars within a 0.40 m beam depth. Tab.3 shows the geometric and mechanical properties of the re-bars before corrosion.

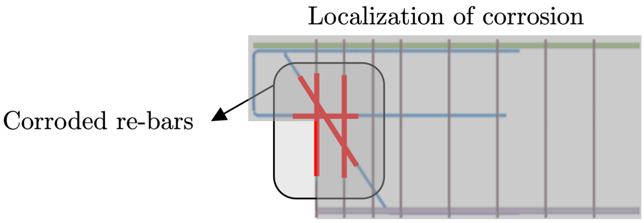

Figure 10: Corrosion localization in the reinforcement layout of the half-joint by Desnerck et al.

Table 3: Geometric and mechanical properties of the re-bars before corrosion.

Re-bars typology	Diameter	Area [mm^2]	f_y	f_u	ϵ_u
Horizontal re-bars	Φ12	113.10	529	600	0.12
Diagonal re-bars	Φ12	113.10	529	600	0.12
Stirrups	Φ10	78.54	539	600	0.12

The authors estimated the force-displacement curve for each level of corrosion from 10 to 50% with a 5% discretization. Fig.11 shows the force-displacement curves in two different scenarios: (a) Reduction of the re-bars cross-section; (b) Reduction of the cross-section and ductility and strength losses.

Table 4: Geometric and mechanical properties of the re-bars for each corrosion level. The resistance values are expressed in kN.

%	$\Phi 10$ [mm^2]	$\Phi 12$ [mm^2]	$\Phi 10$ [mm]	$\Phi 12$ [mm]	$f'_y(\Phi 10)$	$f'_y(\Phi 12)$	$f'_u(\Phi 10\text{-}12)$	ϵ'_u
5	74.61	107.44	4.87	5.85	498.58	489.33	561.00	0.11
10	70.69	101.79	4.74	5.69	458.15	449.65	522.00	0.10
15	66.76	96.13	4.61	5.53	417.73	409.98	483.00	0.09
20	62.83	90.48	4.47	5.37	377.30	370.30	444.00	0.08
25	58.90	84.82	4.33	5.20	336.88	330.63	405.00	0.07
30	54.98	79.17	4.18	5.02	296.45	290.95	366.00	0.06
35	51.05	73.51	4.03	4.84	256.03	251.28	327.00	0.05
40	47.12	67.86	3.87	4.65	215.60	211.60	288.00	0.04
45	43.20	62.20	3.71	4.45	175.18	171.93	249.00	0.03
50	39.27	56.55	3.54	4.24	134.75	132.25	210.00	0.02

- **10% corrosion**: The force-displacement curve related to a 10% corrosion level in Fig.11(a) exhibits a first elastic section with no damage. The first crack arises by the nib, evidenced by the almost horizontal section in the plot. The cracks propagate up to a peak resistance equal to 374 kN corresponding to 9.4 mm, 7% lower than the integer specimen. A softening section follows the horizontal part with consequent failure of the joint. Fig.12 proves that the nib concentrates the cracks. They progress until reaching the upper edge of the beam, where they connect to the other ones.

  In the second scenario with cross-section reduction and ductility loss, a 10% corrosion level is also associated with a ductile behaviour. The first crack arises at 1mm deformation and nearly 200 kN (Fig.11(b)). The curve then exhibits a plastic section followed by a plateau. The cracks localization is analogous to the first scenario with cross-section reduction. The corroded rebars reach the yield stress. Accordingly, the

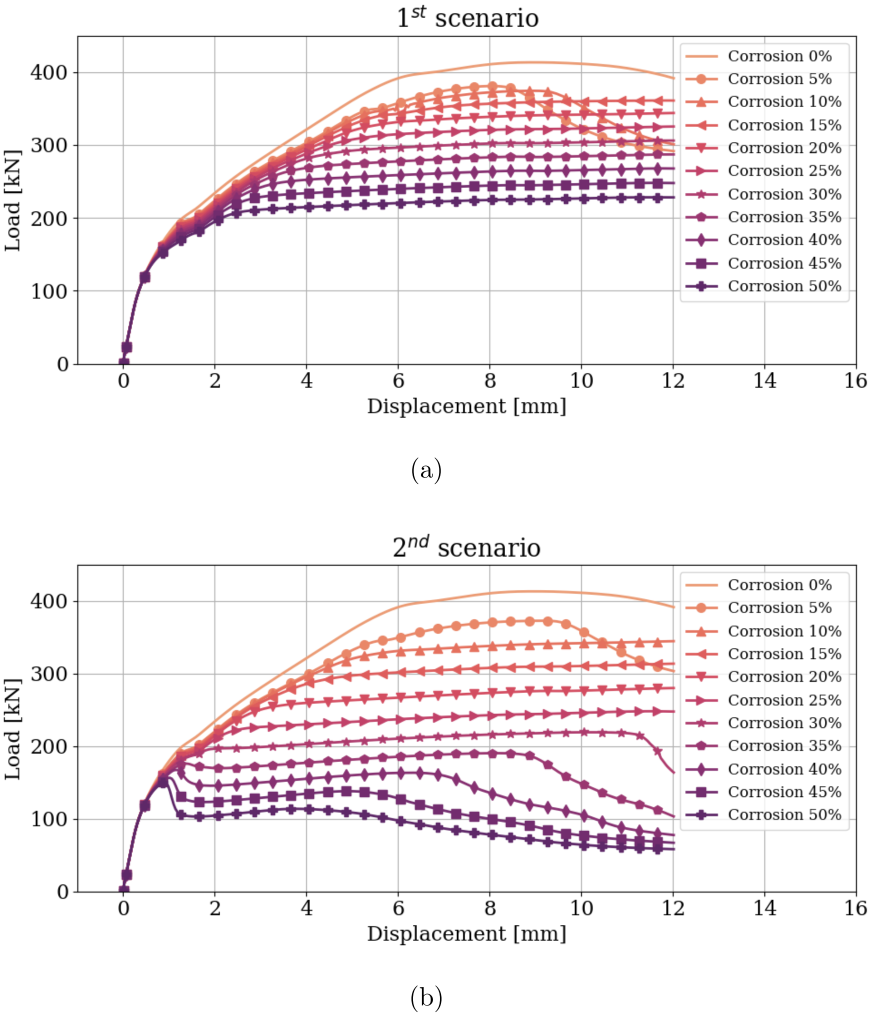

Figure 11: Load-displacement curves as the level of corrosion varies: (a) Reduction of the re-bars cross-section; (b) Reduction of the cross-section and ductility and strength losses.

failure is ductile, being related to the yielding of the corroded rebars.

- **30% corrosion**: The increase in the corrosion level determines a more ductile behaviour, with a first elastic section followed by a plastic branch until reaching a pseudo-plateau at 300 kN (Fig.11(a)). The

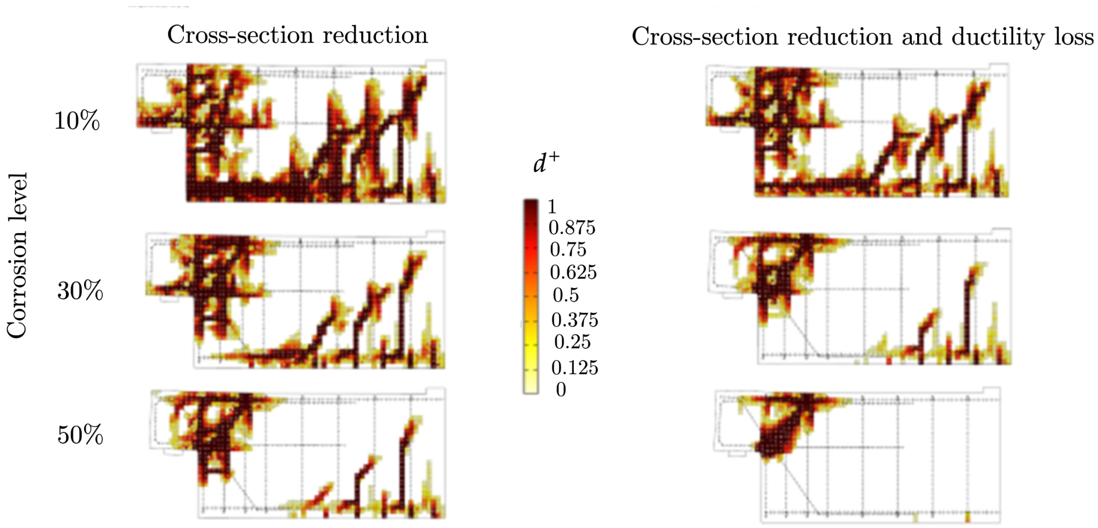

Figure 12: Crack localization at the same load step for different corrosion intensities and the two considered scenarios: cross-section reduction of the re-bars and both cross-section reduction and ductility loss.

crack originates in the nib, reaching the beam's upper edge up to failure. The failure depends on the corroded re-bars yielding, demonstrating the joint ductility. The higher stresses are concentrated in the corroded cross-sections with a tension higher than the yield stress.

In the second scenario with cross-section reduction and ductility loss, a 30% corrosion level leads to a brittle response. Likely, the brittle response is caused by decreased steel's mechanical properties and ductility. First, there is an elastic part, followed by a plastic and hardening phase until reaching approximate 250 kN (Fig.11(b)). Subsequently, the joint strength decreases with increasing displacement until 160kN. The failure depends on the diagonal tension located by the nib. The initial crack grows until the end of the beam is separated. The first three stirrups and the horizontal and diagonal bars have reached the yield point and exceeded the ultimate limit at some points. Therefore, the resistance drop in Fig. 11(b) depends on the collapse of the re-bars.

- **50% corrosion**: A ductile response is also observed for a 50% corrosion level. The load-displacement curve displays an elastic section followed by a plastic one with lower stiffness and a slightly hardening part until a 228kN resistance is reached (Fig.11(a)). The integration stops at 12 mm, set as the maximum displacement threshold. The tensile damage (Fig.12) proves that the failure originates from the diagonal tension spreading from the nib, leading to the detachment of the beam end. The half-joint failure is caused by corroded re-bars yielding, specifically those by the nib and the upper portion of the third stirrups from the beam edge.

  In the second scenario with cross-section reduction and ductility loss, the brittle failure caused by the mechanical properties degradation is even more prominent for a 50% corrosion level. The peak resistance is reached at about 150 kN and 1mm displacement (Fig.11(b)). Subsequently, a resistance drop with ensuing recovery and a final softening section highlighted the half-joint fragile failure. Unlike the previous cases, the cracks are concentrated only by the nib, reaching the beam top with consequent collapse (Fig.12). Similarily to the 30% level, the bars reached the yield condition and, at some points, exceeded the ultimate strength.

4. 2nd case study

The second case study reproduces a half-joint present in an existing viaduct. The joint was modelled considering the entire area of discontinuity or D-Region and a 50cm section of the B-Region. Analogously to the specimen tested by Desnerck et al. [28], the authors carried out a 3D modelling of the joint. The solid model of the half-joint, the load plates and supports are implemented in STKO, and the reinforcement bars and the prestressing cables are modelled with wire elements. For reasons of transverse symmetry, half of the beam is studied by assigning an appropriate constraint configuration. Fig.13 shows some captures of the geometric model in STKO. As illustrated especially in Fig.13 (a) and (c), similarly to the first case study, a continuous steel plate was modeled at the end of the considered B-region also for the viaduct model, where the vertical load is applied. The analysis is conducted with the adaptive LoadControl integrator command until reaching the imposed displacement with 200 incremental steps [31]. The external supports have been modeled as three steel isotropic plates in correspondence with the nib area, where the actual external bearings of the existing viaduct are located.

For concrete, a *DamageTC3D* type nD material is used, which allows grasping the brittle behaviour of the concrete, as well as its tensile and com-

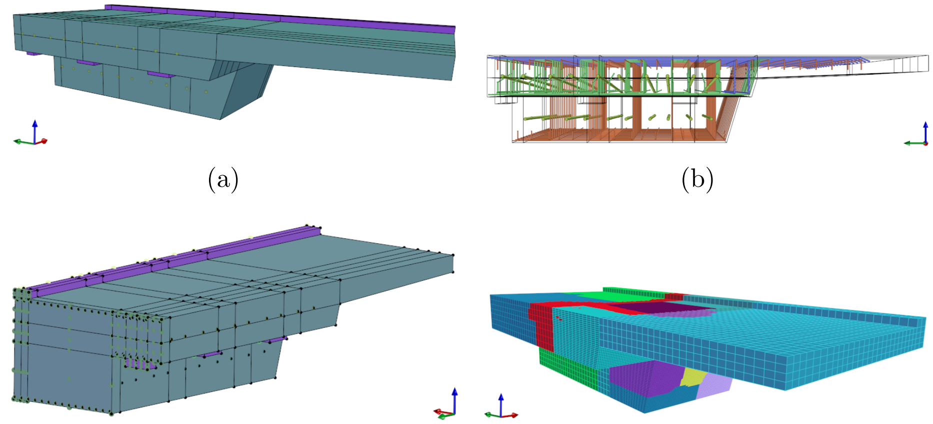

(a) (b)

(c) (d)

Figure 13: (a) 3-d model of the half joint and (b) view of the rebars arrangement; (c) details of the constraint; (d) mesh partition.

pressive response by using the values of the tensile and compressive fracture energy calculated following the Model Code 1990 [37], equal to 21.66 and 0.087 N/mm respectively. The material properties for rebars of the FE model are reported in Table 2 of the present document. A bilinear elastic-hardening behavior is adopted both for rebars and prestressed cables. The pretension of prestressing tendons is modeled as an initial imposed stress applied to tendons beforehand the subsequent incremental analysis starts. The supports and the steel plate where the load is applied are modeled with an elastic material, in a similar way to the first case study. Three mesh typologies are used, *Structured, Linear* and *Hexaedric*. Due to the high computational burden, the mesh size is not constant for the entire structural element. Therefore, a finer mesh is used in the area close to the cross-section reduction equal to 3 cm. A coarser mesh of 9 cm is adopted for the remaining parts. To reduce the computational cost, an analysis is carried out in parallel with multiprocessors, dividing the model into 18 submodels.

4.1. Results in case of no corrosion

Fig.14 shows the force-displacement curve of the half-joint without degradation.

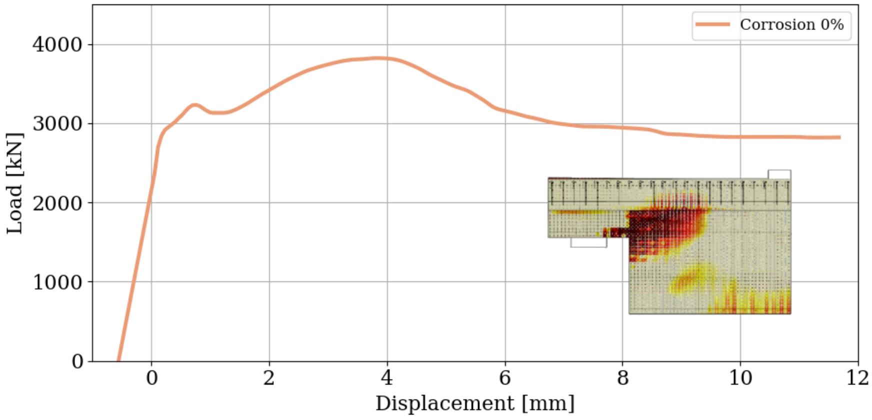

Figure 14: Force-displacement curve of the half-joint without degradation.

After the elastic section, a first resistance peak is reached at 0.75mm displacement, where stirrups' yield occurs. Then, the crack propagation allows reaching a second peak at 3825 kN corresponding to the bearing capacity of the half-joint, following a softening section with a 2800kN plateau. Fig.15 illustrates the analysis results from the initialization of the cracking process to the failure of the specimen. The first crack always arises by the cross-section reduction, with a 45° inclination. The cracking expands in the following loading steps progressing towards the upper edge of the joint.

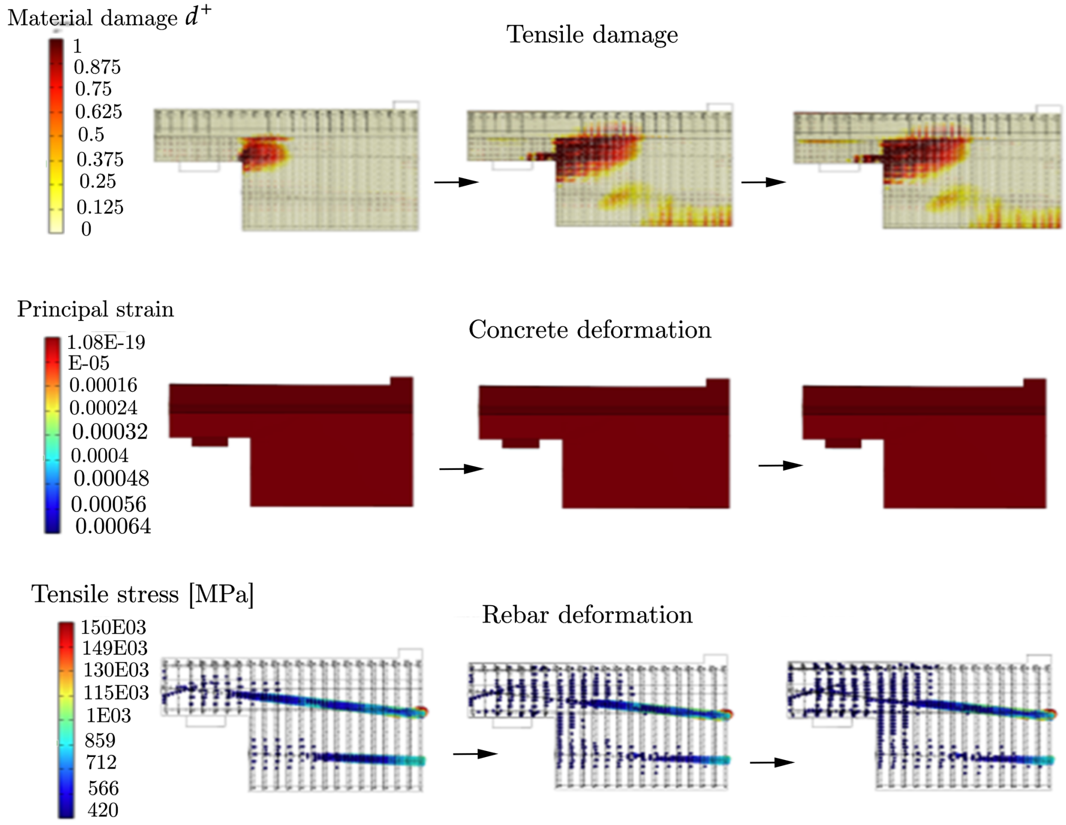

Figure 15: Progress of damage in terms of tensile damage index, concrete deformation and stress in the re-bars.

4.2. Results in case of no corrosion

The same analyses are carried out for the existing viaduct. Corrosion is considered localized in the re-bars highlighted in Fig.16. They include the horizontal bars at the nib, the last stirrups by the nib, the first three stirrups of the entire section and the prestressing cables. The defect is applied homogeneously to all the re-bars for the whole joint thickness.

Tab.5 shows the geometric and mechanical properties of the re-bars before

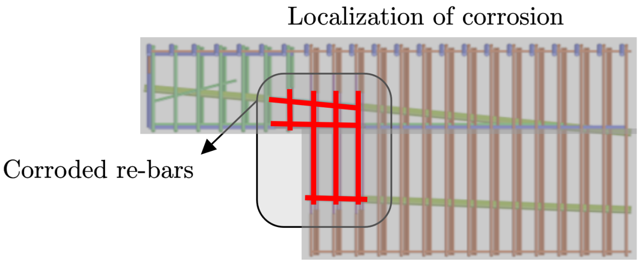

Figure 16: Corrosion localization in the reinforcement layout of the existing half-joint.

corrosion. Similarly, Tab.6 shows the geometric and mechanical properties of the re-bars for each corrosion level. The subscript p indicates the prestressing cables and the resistance values are expressed in mm.

Table 5: Geometric and mechanical properties of the re-bars before corrosion.

Re-bars typology	Diameter	Area [mm^2]	f_y	f_u	ϵ_u
Horizontal re-bars	Φ26	530.929	430	540	0.1
Horizontal re-bars	Φ20	314.159	430	540	0.1
Stirrups	Φ20	314.159	430	540	0.1
Stirrups	Φ16	201.062	430	540	0.1
Prestressing cables	12x0.6”	2188.976	1620	1800	0.2

Fig.17 illustrates the damage pattern for increasing levels of corrosion in the two scenarios: (1st) cross-section reduction and (2nd) cross-section reduction and steel degradation. The corresponding force-displacement curves for the two scenarios are shown in Fig.18.

In details:

- **10% corrosion**:The load-displacement curve does not display observable variations compared to the case without corrosion. After the elastic phase, a first local peak is reached at nearly 3400 kN, followed by

Table 6: Geometric and mechanical properties of the re-bars for each corrosion level. The subscript p indicates the prestressing cables and the resistance values are expressed in kN.

%	Φ cables [mm]	Φ16 [mm]	Φ20 [mm]	Φ26 [mm]	f'_{yp}	f'_y	f'_{up}	f'_u	ϵ'_{up}	ϵ'_u
5	51.5	15.6	19.5	25.3	1499	398	1683	505	0.14	0.11
10	50.1	15.2	19	24.7	1377	366	1566	470	0.12	0.10
15	48.7	14.8	18.4	24	1256	333	1449	435	0.11	0.09
20	47.2	14.3	17.9	23.3	1134	301	1332	400	0.10	0.08
25	45.7	13.9	17.3	22.5	1013	269	1215	365	0.09	0.07
30	44.2	13.4	16.7	21.8	891	237	1098	329	0.07	0.06
35	42.6	12.9	16.1	21	770	204	981	294	0.06	0.05
40	40.9	12.4	15.5	20.1	648	172	864	259	0.05	0.04
45	39.2	11.9	14.8	19.3	527	140	747	224	0.04	0.03
50	37.3	11.3	14.1	18.4	405	108	630	189	0.02	0.02

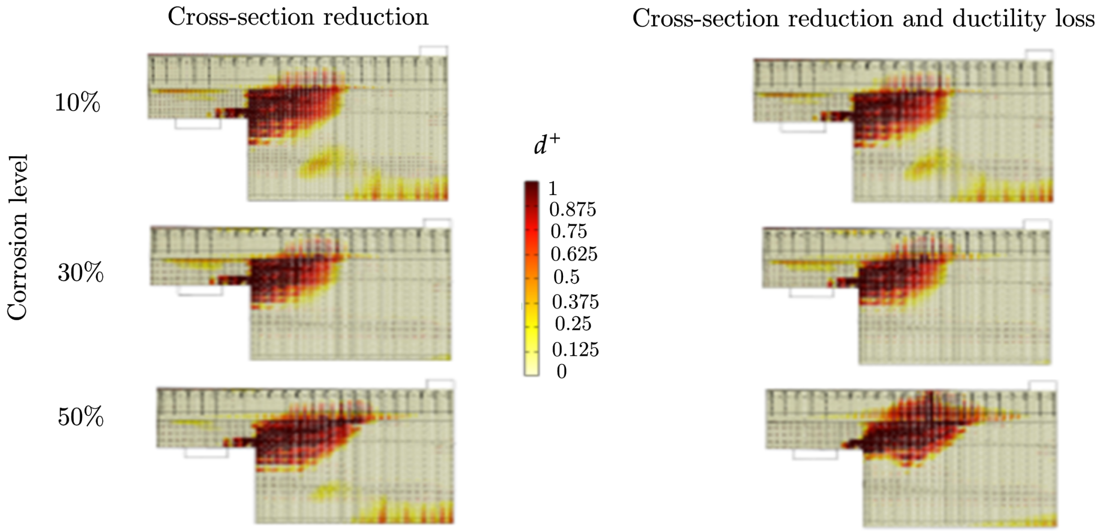

Figure 17: Crack localization for different corrosion intensities and the two considered scenarios: cross-section reduction of the re-bars and both cross-section reduction and ductility loss of steel.

a slight strength drop with subsequent recovery up to the global peak of 3800 kN (Fig.18(a)). The curve then exhibits a minor softening until the plateau at 2800 kN. The crack pattern is mainly located by the cross-section variation, as shown in (Fig.17). The concrete defor-

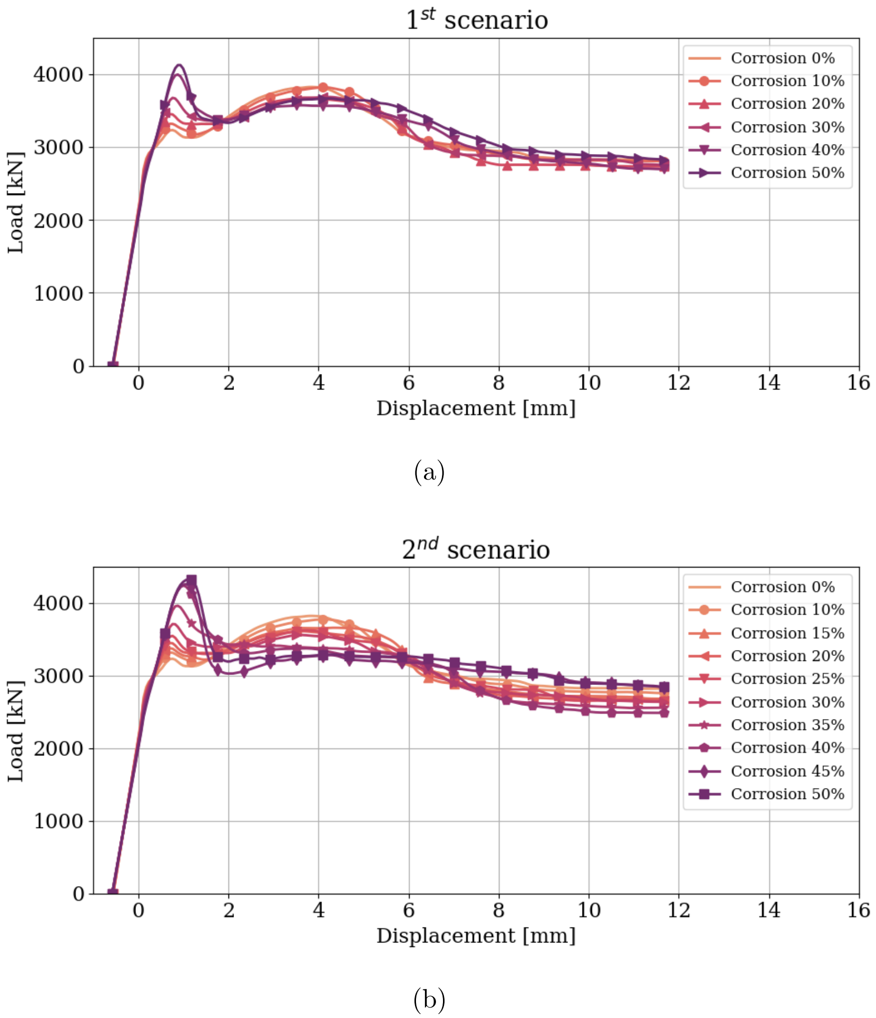

(a)

(b)

Figure 18: Load-displacement curves as the level of corrosion varies: (a) Reduction of the re-bars cross-section; (b) Reduction of the cross-section and ductility and strength losses.

mation does not exceed the critical value of 0.35%. Conversely, the stirrups in the nib and the first stirrups of the whole section reach the yielding stresses. The variation of the constitutive behaviour of steel does not affect the response of the half-joint for a corrosion level equal to 10% (Fig.18(b)). Therefore, the load-displacement curve shows the same trend observed in the first scenario when the sole cross-section reduction describes corrosion.

- **30% corrosion**: With a 30% corrosion level, there is an increase in the first peak from 3400 kN to about 3600 kN. On the other hand, the second peak experiences a 3% decrease, followed by a weakly softening branch until reaching the plateau (Fig.18(a)). In the second scenario, characterized by cross-section reduction and material degradation, a corrosion level equal to 30% leads to a less ductile behaviour. As a result, the force-displacement curve exhibits a first elastic phase until reaching the first peak at about 3600 kN. Then, an overall softening behaviour is associated with a marked resistance reduction in the second local peak (Fig.18(b)).
- **50% corrosion**: The half-joint with a 50% corrosion level exhibits an elastic phase up to a peak resistance close to 4050 kN. There is a slight softening behaviour in a second phase with a minor resistance recovery between 2 and 4 mm. A second lower peak arises at approximately 3800 kN. In the second scenario, the embrittlement of the response is even more evident in the case of 50% corrosion. After a 4200 kN peak, a sudden resistance drop occurs, followed by a pseudo plateau at 3000 kN.

5. Discussion and comparison between case studies

The paper investigates the force-displacement response of two half-joints, the one tested by Desnerck et al. also used for the model validation and an existing half-joint. The effects of corrosion on the two joints are considered separately by modelling the cross-section reduction and steel degradation. The results corresponding to three corrosion levels (10%, 30% and 50%) demonstrate that corrosion affects the bearing capacity and failure modes.

Fig.11 shows the load-displacement curves for increasing corrosion intensities in the half-joint considered by Desnerck et al. The simulations of the first scenario (cross-section reduction) highlight a notable strength reduction with a pseudo-plateau after the force peak. In addition, the section reductions of 5% and 10% induce a more brittle behaviour due to the softening branch after the force peak before reaching the plateau. Conversely, higher levels of corrosion determine a more ductile response. Still, the peak resistance is slightly lower than that observed by the displacement threshold, set equal to 12 mm. There is an almost linear variation of the bearing capacity with a good adherence with the results by Desnerck [67]. Desnerck studied the corrosion of several re-bars that exhibited an approximately 20% strength reduction with a corrosion percentage equal to 40%. In these analyses, a 37% strength reduction corresponded to a corrosion percentage similar to 40%. Additionally, the failure modes vary with the rate of corrosion. Low corrosion levels lead to a shear failure affecting the entire cross-section, where the cracks initiate from the internal corner of the nib and fuse to the shear and bending cracks of the full section beam. Higher percentages of corrosion lead to shear failure due to the high diagonal tension. The cracks in the nib arise from the beam's upper edge causing a detachment. The re-bars with reduced cross-section reach the yield stress. There are no compression cracks since the bars' yielding always foregoes the concrete breaking. Interestingly, the 5% and 10% corrosion levels show a counterintuitive phenomenon. The cracks pattern directs to a detachment of the concrete cover at the lower edge, generating a resistance drop after the peak. The steel's loss of ductility and strength determines a more fragile response. These phenomena can be observed from the direct inspection of Fig.11.

In the second scenario, where the cross-section reduction and the steel degradation occur, the bearing capacity decrease is more marked and less linear. A 50% corrosion level leads to a 72% strength drop. The structure reveals a ductile behaviour up to 25% corrosion level, except for the 5% case where, as in the first scenario, a post-peak softening phase occurs. A more fragile response is observed for higher corrosion levels (starting from 30%). This fact depends on the strength and ductility degradation of steel. The first stirrups and the diagonal bars exceed the ultimate strength and exhibit a resistance decrement associated with softening branch before the collapse. An increase in the percentage of corrosion cause the beam detachment due to the diagonal crack in the nib.

The second case study refers to an half- joint of an existing viaduct. The authors simulated the corrosion effects by reducing the cross-section from

10% to 50% with 10% steps. Fig.18 shows the load-displacement curves for different corrosion levels in two scenarios, the first simulating the cross-section reduction, while the second also includes the steel degradation. The curves have a similar trend: a first elastic section ends with the first local resistance peak. Then, a plastic stage culminates with a second local peak, followed by a softening and a final pseudo plateau. In the present case study, there is no noticeable variation in the overall resistance of the joint. However, the first resistance peak exhibits a 22% increment in case of corrosion percentage equal to 50%. Conversely, the second resistance peak experiences an approximate 5% reduction. The joint always shows a high bearing capacity with slight embrittlement of failure mode. Since the 30% corrosion level, the maximum resistance corresponds to the end of the elastic phase with a 1mm displacement. Subsequently, the response has a softening branch, achieving a pseudo-plateau at approximately 2800 kN. The Gerber joint for each corrosion percentage displays an approximately 45 ° inclined crack, which initiates from the internal edge and continues towards the wing of the viaduct. As a result, the stirrups always yield in the cross-section reduction, while the concrete does not exceed the 0.35% critical deformation. In the second scenario, the corrosion is modelled regarding cross-section reduction and ductility loss. Also, in this case, the overall resistance is not significantly affected. However, at the same time, there is more evident embrittlement of the structural response with a 16% reduction of the second local peak and a more pronounced softening for a 50% corrosion level.

The first case study has been considerably studied in scientific literature, e.g. [16, 28]. Therefore, the advantages of studying Desnerck's beam offered the possibility to calibrate the proposed methodology, at least validating the uncorroded case, based on experimental results obtained by Desnerck et al. [28]. The calibration procedure permitted the identification of the Model Code 1990 formulations for fracture energy, and consequently for the other mechanical parameters, to provide the best matching with the experimental curve [28]. Based on these results, the authors extended and transpose these considerations of Model Code 1990 formulations also to the second case study, which on the contrary appears less studied in scientific literature. Thus, this highlights how real-world and non-conventional Gerber half-joint structural layouts, even considering prestressing conditions, should be further explored. Furthermore, performing a comparison between the two different case studies of the present document, despite a different structural configuration, scenario 2 pointed out a general embrittlement behavior for corrosion levels over 30% for both case studies. Scenario 1 in Desnerck's beam illustrated a reduction in terms of capacity only with the increase of corrosion level, maintaining an almost ductile behavior up to the maximum imposed displacement. On the contrary, for scenario 1, the second case study presents a decrease of the peak strength up to 30% of corrosion, with a more brittle behavior for higher corrosion levels. This fact may enlighten that for prestressed reinforced concrete structures it would be more plausible a brittle mechanism for an advanced corrosion situation.

In summary, it is worth noting that the results provided in the current study may be representative of real-world situations only for corrosion levels up to 30% of cross section reduction, which are typically the maximum values hitherto observed in normal environmental exposure conditions [68, 69]. However, some research studies pointed out how chloride attacks and subsequent pitting corrosion may reach also a cross-section reduction up to 50% [70]. On the other hand, considering experimental campaigns with artificially induced accelerated corrosion, such as [71], it appears evident as in the scientific literature a cross section reduction of 50% represents a sort of boundary, beyond which it is no more a realistic behavior to investigate. Therefore, in the current study, the author's goal was to explore the half-joint behavior in terms of capacity and ductility considering numerical simulation up to 50% of cross section reduction, being conscious that the representativeness of the results may be transposed to real-world problems only up to about 30%. As a matter of fact, for high levels of corrosion, it is more probable that the severe crack pattern coupled with the effect of the expansive nature of products of advanced corrosion may induce other phenomena such as concrete spalling, or rebar slippage, which are far from the hypothesis of the current numerical simulations. Thus, future research studies may involve the calibration of more sophisticated adhesion models in order to attempt to capture these phenomena induced by high corrosion levels. Therefore, it is worth noting that the peculiar first peak resistance increase presented in the second analyzed case study (see Fig. 18) becomes relevant for corrosion levels above the virtually realistic value of 30% of cross section reduction. This particular behavior may probably be related to the simplified modeling assumptions, which in the present study disregard possible slippage phenomena due to adhesion loss for the corrosion, or concrete spalling phenomena. In particular, the occurrence of this latter may directly affect the capacity due to a sudden reduction of a cross-section and it will probably mitigate the first peak resistance increase. However, since the current study focused especially on how the ductility and/or strength reduction of corroded bars may affect the overall behavior of the half-joint, if the considered half-joint would be virtually able to reach a high corrosion level under the current modeling assumptions, the resulting behavior would have pointed out a substantial embrittlement, for both scenarios 1 and 2.

6. Conclusions

Gerber's joints are notably vulnerable to the attack of corrosive agents. The rainwater from the deck and the de-icing salts without adequate drainage systems can trigger corrosion. Likewise, the geometry of the Gerber's joints does not allow easy inspection of the nib. Therefore, the degradation induced by corrosion is particularly crucial for Gerber's joints. The research focused on the Finite Element modelling in OpenSees STKO and the non-linear analysis of two case studies subject to corrosion. The first case study is a Gerber joint tested by Desnerck et al. [28]. On the other hand, the second case corresponds to a joint of an existing viaduct. Initially, the authors estimated the behaviour in the absence of corrosion by validating the model with the experimental tests by Desnerck et al. [28]. The comparisons between the two case studies without corrosion highlight the more rigid behaviour of the existing joint compared to the Desnerck case. The cracks locations, the tension in the reinforcing bars and the minimum deformation of the concrete contribute to a ductile failure mode. The corrosion was investigated in two scenarios: cross-section reduction and both cross-section reduction and ductility loss. The analysis estimated the effects of increasing corrosion levels from 5% to 50% with 5% steps. The Desnerck joint showed a linear decrease of the bearing capacity as the corrosion level increased. This fact, which originated from the cross-section reduction, was accompanied by embrittlement of the response in the second scenario. On the contrary, the existing joint did not reveal an appreciable variation in resistance but rather global embrittlement of the behaviour.

Acknowledgments

The authors kindly acknowledge the contribution given by Guido Camata and Massimo Petracca for the academic license of STKO software and for the fundamental support in developing the present work. The authors acknowledge Davide Masera for suggesting the real case study bridge and providing the necessary information for modeling purposes. The authors acknowledge particularly Giuseppe Carlo Marano for his supervision in the present work.

References

[1] J. Mathivat, The cantilever construction of prestressed concrete bridges, Wiley, 1984.

[2] P. Desnerck, J. M. Lees, C. Morley, Assessment of reinforced concrete half-joint structures: dealing with deterioration (2014).

[3] Z. Šauman, Carbonization of porous concrete and its main binding components, Cement and Concrete Research 1 (6) (1971) 645–662.

[4] H. M. Abdul-Jawad, Modelling of dapped-end beams using abaqus software (2018).

[5] M. Kashani, J. Maddocks, E. Afsar Dizaj, Residual capacity of corroded reinforced concrete bridge components: a state-of-the-art review, Journal of Bridge Engineering 24 (7) (2019) 1–16.

[6] A. Pelle, B. Briseghella, A. V. Bergami, G. Fiorentino, G. F. Giaccu, D. Lavorato, G. Quaranta, A. Rasulo, C. Nuti, Time-dependent cyclic behavior of reinforced concrete bridge columns under chlorides-induced corrosion and rebars buckling, Structural Concrete 23 (1) (2022) 81–103.

[7] D. Lavorato, G. Fiorentino, A. Pelle, A. Rasulo, A. V. Bergami, B. Briseghella, C. Nuti, A corrosion model for the interpretation of cyclic behavior of reinforced concrete sections, Structural Concrete 21 (5) (2020) 1732–1746.

[8] P. Desnerck, J. M. Lees, P. Valerio, N. Loudon, C. T. Morley, Inspection of rc half-joint bridges in england: analysis of current practice, in: Proceedings of the Institution of Civil Engineers-Bridge Engineering, Vol. 171, Thomas Telford Ltd, 2018, pp. 290–302.

[9] T. A. Nicholson, Design and construction of a34 wolvercote highway viaduct replacement, uk, in: Proceedings of the Institution of Civil Engineers-Bridge Engineering, Vol. 167, Thomas Telford Ltd, 2014, pp. 122–130.

[10] A. Pelle, B. Briseghella, G. Fiorentino, G. F. Giaccu, D. Lavorato, G. Quaranta, A. Rasulo, C. Nuti, Repair of reinforced concrete bridge columns subjected to chloride-induced corrosion with ultra-high performance fiber reinforced concrete, Structural Concrete (2022).

[11] F. Totani, A. Aloisio, D. Ranalli, G. Totani, Field investigation on the reinforcing steel corrosion of rc infrastructures in abruzzo, in: International Conference of the European Association on Quality Control of Bridges and Structures, Springer, 2021, pp. 971–978.

[12] D. Smith, Refurbishment of the old medway bridge, uk, in: Proceedings of the Institution of Civil Engineers-Bridge Engineering, Vol. 158, Thomas Telford Ltd, 2005, pp. 129–139.

[13] G. Santarsiero, A. Masi, V. Picciano, Durability of gerber saddles in rc

bridges: Analyses and applications (musmeci bridge, italy), Infrastructures 6 (2) (2021) 25.

[14] A. I. Quadri, C. Fujiyama, Response of reinforced concrete dapped-end beams exhibiting bond deterioration subjected to static and cyclic loading, Journal of Advanced Concrete Technology 19 (5) (2021) 536–554.

[15] D. Mitchell, J. Marchand, P. Croteau, W. D. Cook, Concorde overpass collapse: structural aspects, Journal of performance of constructed facilities 25 (6) (2011) 545–553.

[16] N. Chijiwa, B. Suryanto, R. Kurihara, Forensic analysis of reinforced concrete half-joints, Technology 6 (1) 215–226.

[17] P. Desnerck, J. M. Lees, C. T. Morley, Strut-and-tie models for deteriorated reinforced concrete half-joints, Engineering Structures 161 (2018) 41–54.

[18] M. Petracca, F. Candeloro, G. Camata, Stko user manual, ASDEA Software Technology: Pescara, Italy (2017).

[19] M. P. Collins, Towards a rational theory for rc members in shear, Journal of the Structural Division 104 (4) (1978) 649–666.

[20] J. Schlaich, K. Schäfer, M. Jennewein, Toward a consistent design of structural concrete, PCI journal 32 (3) (1987) 74–150.

[21] A. Committee, Building code requirements for structural concrete (aci 318-08) and commentary, American Concrete Institute, 2008.

[22] M. Di Ludovico, A. Prota, G. Manfredi, E. Cosenza, Frp strengthening of full-scale pc girders, Journal of Composites for Construction 14 (5) (2010) 510–520.

[23] E. Mörsch, Concrete-steel construction (der Eisenbetonbau), Engineering news publishing Company, 1909.

[24] A. K. Seite, Die bauweise hennebique.*, Schweizerische Bauzeitung 33 (1899) 41.

[25] A. H. Mattock, Design proposals for reinforced concrete corbels, PCI journal 21 (3) (1976) 18–42.

[26] S. K. Liem, Maximum shear strength of dapped-end or corbel, Ph.D. thesis, Concordia university (1983).

[27] W.-Y. Lu, I.-J. Lin, S.-J. Hwang, Y.-H. Lin, Shear strength of high-strength concrete dapped-end beams, Journal of the Chinese Institute of Engineers 26 (5) (2003) 671–680.

[28] P. Desnerck, J. M. Lees, C. T. Morley, Impact of the reinforcement layout on the load capacity of reinforced concrete half-joints, Engineering Structures 127 (2016) 227–239.

[29] G. Quaranta, D. De Domenico, G. Monti, Machine-learning-aided improvement of mechanics-based code-conforming shear capacity equation for rc elements with stirrups, Engineering Structures 267 (2022) 114665.

[30] F. Tariq, P. Bhargava, Stress–strain curves and mechanical properties of corrosion damaged super ductile reinforcing steel, Structures 33 (2021) 1532–1543. `doi:https://doi.org/10.1016/j.istruc.2021.05.039`. URL `https://www.sciencedirect.com/science/article/pii/S2352012421004422`

[31] S. Mazzoni, F. McKenna, M. H. Scott, G. L. Fenves, et al., Opensees command language manual, Pacific Earthquake Engineering Research (PEER) Center 264 (1) (2006) 137–158.

[32] A. Hillerborg, M. Modéer, P.-E. Petersson, Analysis of crack formation and crack growth in concrete by means of fracture mechanics and finite elements, Cement and concrete research 6 (6) (1976) 773–781.

[33] A. Saetta, R. Scotta, R. Vitaliani, Coupled environmental-mechanical damage model of rc structures, Journal of engineering mechanics 125 (8) (1999) 930–940.

[34] M. Petracca, L. Pelà, R. Rossi, S. Zaghi, G. Camata, E. Spacone, Micro-scale continuous and discrete numerical models for nonlinear analysis of masonry shear walls, Construction and Building Materials 149 (2017) 296–314.

[35] J. Oliver, A consistent characteristic length for smeared cracking models, International Journal for Numerical Methods in Engineering 28 (2) (1989) 461–474.

[36] Z. P. Bažant, B. H. Oh, Crack band theory for fracture of concrete, Matériaux et construction 16 (3) (1983) 155–177.

[37] L. Taerwe, S. Matthys, et al., Fib model code for concrete structures 2010 (2013).

[38] P. Castaldo, D. Gino, G. Bertagnoli, G. Mancini, Resistance model uncertainty in non-linear finite element analyses of cyclically loaded reinforced concrete systems, Engineering Structures 211 (2020) 110496.

[39] C. Lassi, Studio con il metodo degli elementi finiti dell'accoppiamento forzato ruota sala ferroviaria, Master Thesis, AA 1994-1995, Dipartimento di Meccanica, Politecnico di Milano (1995).

[40] K.-J. Bathe, Finite element procedures prentice-hall, New Jersey 1037 (1996) 1.

[41] H. Lee, F. Tomosawa, T. Noguchi, Effects of rebar corrosion on the structural performance of singly reinforced beams, in: Durability of Building Materials and Components 7, Routledge, 2018, pp. 571–580.

[42] S. J. Williamson, L. A. Clark, Effect of corrosion and load on reinforcement bond strength, Structural engineering international 12 (2) (2002) 117–122.

[43] D. V. Val, M. G. Stewart, R. E. Melchers, Effect of reinforcement corrosion on reliability of highway bridges, Engineering structures 20 (11) (1998) 1010–1019.

[44] M. G. Stewart, D. V. Rosowsky, Time-dependent reliability of deteriorating reinforced concrete bridge decks, Structural safety 20 (1) (1998) 91–109.

[45] E. Dizaj, J. Padgett, M. Kashani, A markov chain-based model for structural vulnerability assessmentof corrosion-damaged reinforced concrete bridges, Philosophical Transactions of the Royal Society A: Mathematical, Physical and Engineering Sciences 379 (2203), cited By 6 (2021). `doi:10.1098/rsta.2020.0290`.

[46] N. Lethanh, J. Hackl, B. Adey, Estimating markov transition probabilities for reinforced concrete bridges based on mechanistic-empirical corrosion models, 2016, pp. 1915–1922, cited By 0.

[47] J. Zhao, D.-T. Niu, Corrosion cracking time models sensitivity of reinforced concrete bridge, Chang'an Daxue Xuebao (Ziran Kexue Ban)/Journal of Chang'an University (Natural Science Edition) 34 (6) (2014) 107–116, cited By 1.

[48] P. Marsh, D. Frangopol, Reinforced concrete bridge deck reliability model incorporating temporal and spatial variations of probabilistic cor-

rosion rate sensor data, Reliability Engineering and System Safety 93 (3) (2008) 394–409, cited By 108. `doi:10.1016/j.ress.2006.12.011`.

[49] B. Yu, L. Yang, M. Wu, B. Li, Practical model for predicting corrosion rate of steel reinforcement in concrete structures, Construction and Building Materials 54 (2014) 385–401, cited By 74. `doi:10.1016/j.conbuildmat.2013.12.046`.

[50] F. Xu, Y. Xiao, S. Wang, W. Li, W. Liu, D. Du, Numerical model for corrosion rate of steel reinforcement in cracked reinforced concrete structure, Construction and Building Materials 180 (2018) 55–67, cited By 30. `doi:10.1016/j.conbuildmat.2018.05.215`.

[51] X. Chen, Q. Zhang, P. Chen, Q. Liang, Numerical model for local corrosion of steel reinforcement in reinforced concrete structure, Computers and Concrete 24 (4) (2021) 385–393, cited By 1. `doi:10.12989/cac.2021.27.4.385`.

[52] W. Zhu, K. Yu, Y. Xu, K. Zhang, X. Cai, A prediction model of the concrete cracking induced by the non-uniform corrosion of the steel reinforcement, Materials 13 (4), cited By 5 (2020). `doi:10.3390/ma13040830`.

[53] B. Sun, R.-C. Xiao, W.-D. Ruan, P.-B. Wang, Corrosion-induced cracking fragility of rc bridge with improved concrete carbonation and steel

reinforcement corrosion models, Engineering Structures 208, cited By 16 (2020). `doi:10.1016/j.engstruct.2020.110313`.

[54] K. Zhang, J. Xiao, Y. Zhao, Q. Zhang, Analytical model for critical corrosion level of reinforcements to cause the cracking of concrete cover, Construction and Building Materials 223 (2019) 185–197, cited By 15. `doi:10.1016/j.conbuildmat.2019.06.210`.

[55] S. Morinaga, Remaining life of reinforced concrete structures after corrosion cracking, in: Durability of Building Materials and Components 7, Routledge, 2018, pp. 127–136.

[56] I. M. Allam, M. Maslehuddin, H. Saricimen, A. I. Al-Mana, Influence of atmospheric corrosion on the mechanical properties of reinforcing steel, Construction and Building Materials 8 (1) (1994) 35–41.

[57] R. Palsson, M. S. Mirza, Mechanical response of corroded steel reinforcement of abandoned concrete bridge, Structural Journal 99 (2) (2002) 157–162.

[58] G. C. Marano, G. Quaranta, M. Mezzina, Fuzzy time-dependent reliability analysis of rc beams subject to pitting corrosion, Journal of Materials in Civil Engineering 20 (9) (2008) 578–587.

[59] M. G. Stewart, A. Al-Harthy, Pitting corrosion and structural reliability of corroding rc structures: Experimental data and probabilistic analysis, Reliability engineering & system safety 93 (3) (2008) 373–382.

[60] M. Maslehuddin, I. A. Allam, G. J. Al-Sulaimani, A. Al-Mana, S. N. Abduljauwad, Effect of rusting of reinforcing steel on its mechanical properties and bond with concrete, Materials Journal 87 (5) (1990) 496–502.

[61] A. Castel, R. François, G. Arliguie, Mechanical behaviour of corroded reinforced concrete beams—part 1: Experimental study of corroded beams, Materials and Structures 33 (9) (2000) 539–544.

[62] C. A. Apostolopoulos, V. Papadakis, Consequences of steel corrosion on the ductility properties of reinforcement bar, Construction and Building Materials 22 (12) (2008) 2316–2324.

[63] J. Cairns, Y. Du, D. Law, Residual bond strength of corroded plain round bars, Magazine of Concrete Research 58 (4) (2006) 221–231.

[64] J. Cairns, G. A. Plizzari, Y. Du, D. W. Law, C. Franzoni, Mechanical properties of corrosion-damaged reinforcement, ACI Materials Journal 102 (4) (2005) 256.

[65] C. Andrade, C. Alonso, D. Garcia, J. Rodriguez, Remaining lifetime of reinforced concrete structures: Effect of corrosion on the mechanical properties of the steel (1991).

[66] S. A. Abeysinghe, H. D. Yapa, Numerical simulation of damaged reinforced concrete half-joint beams: towards appraisal and retrofitting,

Proceedings of the Institution of Civil Engineers-Structures and Buildings (2022) 1–37.

[67] P. Desnerck, J. Lees, C. Morley, Impact of material deterioration on the strength of reinforced concrete half-joint structures (2015).

[68] C. Fu, N. Jin, H. Ye, X. Jin, W. Dai, Corrosion characteristics of a 4-year naturally corroded reinforced concrete beam with load-induced transverse cracks, Corrosion Science 117 (2017) 11–23.

[69] A. Dasar, H. Hamada, Y. Sagawa, D. Yamamoto, Deterioration progress and performance reduction of 40-year-old reinforced concrete beams in natural corrosion environments, Construction and Building Materials 149 (2017) 690–704.

[70] V. H. Dang, R. François, Influence of long-term corrosion in chloride environment on mechanical behaviour of rc beam, Engineering Structures 48 (2013) 558–568.

[71] W. Zhu, R. Francois, Experimental investigation of the relationships between residual cross-section shapes and the ductility of corroded bars, Construction and Building Materials 69 (2014) 335–345.